RSC Advances

ROYAL SOCIETY OF CHEMISTRY

PAPER

View Article Online
View Journal | View Issue

Check for updates

Cite this: *RSC Adv.*, 2025, **15**, 38636

Boosting energy storage density of lithium-ion hybrid capacitors *via* 3D graphene nanoflake integration

Yu-Han Chou,[a] Wan-Ying Wu,[b] Jia-De Wei,[b] Ting-Wei Wu[c] and Wei-Shiuan Tseng *[a]

Received 10th September 2025
Accepted 26th September 2025

DOI: 10.1039/d5ra06831b

rsc.li/rsc-advances

To meet the growing global energy demand across applications such as electric vehicles, mobile devices, and household electricity, lithium-ion hybrid capacitors (LIHCs) offer a more ingenious design than traditional lithium-ion batteries or supercapacitors, delivering superior performance in both energy and power density. The introduction of conductive additives into activated carbon-based electrodes is an advanced strategy to further enhance the performance of energy storage devices. In this study, we demonstrate the integration of 3D graphene nanoflakes (GNFs) into LIHCs to achieve promising charge storage characteristics. GNFs in this work were synthesized *via* an efficient and environmentally friendly approach and integrated into LIHCs as an additive. Unlike conventional chemical vapor deposition (CVD), the proposed plasma-enhanced CVD technique enables the synthesis of highly conductive GNFs with controlled surface area and 3D architecture at much lower temperatures (<300 °C) in just 10 minutes, without the need for toxic gases or additional catalysts. The as-synthesized GNFs possess a uniform open 3D network with high conductivity, structural stability, as well as intrinsic hydrophilicity. With the assistance of GNFs, the LIHC exhibited substantial improvements in both capacity and energy density. The device incorporating 2.5 wt% GNF achieved an impressive capacity of 62.35 mAh g^{-1}, along with advanced energy density of 115.58 Wh kg^{-1}. These results surpass LIHCs with commercial Super P and achieve higher energy density than most reported LIHCs with similar architectures and electrodes. The optimized LIHC even demonstrates energy densities beyond the conventional limits of LIHCs, entering the performance regime of lithium-ion batteries. This study provides a clean and efficient approach that paves the way for next-generation LIHCs, delivering excellent energy densities without compromising power density.

1. Introduction

Due to the surge in global energy demand, a wide range of high-performance energy storage approaches, such as electric double-layer capacitors (EDLCs) and lithium-ion batteries (LIBs), have been actively developed over the past decades.[1–3] EDLCs, constructed with positive/negative electrode, electrolyte, and separator possess high power density as well as excellent charge/discharge stability.[3] Materials with high specific surface area are commonly selected as electrodes such as activated carbon and carbon nanotubes.[4] Electrolytes based on organic, aqueous, and ionic liquids have been explored, with organic types being generally preferred due to their relatively high conductivity and operating voltage (2–3 volts).[5] While supercapacitors offer high power density and long cycle life, LIBs, on the other hand, exhibit significantly higher energy density. Applications requiring high charge capacity, such as electric vehicles and mobile phone batteries, currently rely on LIBs as the primary energy storage units. To meet the ever-growing energy demand, the lithium-ion hybrid capacitor (LIHC) offers a more advanced design, delivering promising performance in both energy density and power density.[6,7] LIHCs utilize one lithium electrode and one double-layer capacitor with different properties—one featuring electrostatic capacitance and the other electrochemical capacitance—effectively combining the advantages of EDLCs and pseudo-capacitors, such as rapid charge/discharge and abundant capacity.[8] The charge storage mechanism of lithium battery-type electrodes (typically cathodes) relies on ion intercalation/deintercalation and is composed of a mixture of lithium iron phosphate and carbon-based materials with high theoretical specific capacity.[9]

---

[a] *Institute of Imaging and Biomedical Photonics, College of Photonics, National Yang-Ming Chiao-Tung University, Tainan 71150, Taiwan. E-mail: wstseng@nycu.edu.tw*

[b] *Institute of Lighting and Energy Photonics, College of Photonics, National Yang-Ming Chiao-Tung University, Tainan 71150, Taiwan*

[c] *Institute of Photonic System, College of Photonics, National Yang-Ming Chiao-Tung University, Tainan 71150, Taiwan*

Activated carbon is widely used for carbon-based electrode material due to its high specific surface area, enabling excellent charge storage capacity.[10] In addition to activated carbon, a variety of carbon-based materials have been developed and explored in recent years as electrode materials or additives to overcome the functional limitations of conventional pure activated carbon electrodes in batteries and capacitors.[11,12] Among them, conductive carbon materials such as carbon black,[13] graphite,[14] hard carbon,[15] carbon nano-tubes,[16] activated carbon,[17] and graphene,[18] have demonstrated promising performance due to their various excellent functionaities.[19] For example, carbon blacks are tiny particles formed through a low-oxygen decomposition process at high temperatures, resulting in a high specific surface area that significantly improves the transport efficiency of slurry.[13] Carbon nanotubes are hollow, tube-shaped materials composed of carbon atoms usually made from wrapped graphene. Due to their high aspect ratio and great strength, they can serve as conductive bridges within electrodes, enhancing electrical conductivity.[16] More importantly, as a highly attention-attracting material of the 21st century, graphene also plays a significant role in electrodes due to its exceptional electrical conductivity.[18] The tightly bonded σ along with delocalized π electrons in graphene enable ultra-high electron mobility due to ballistic transport. Additionally, its outstanding mechanical strength and thermal conductivity contribute to its superior performance across various applications.[19–22]

In this study, we firstly demonstrate the integration of 3D graphene nanoflakes (GNFs) into LIHCs to achieve promising charge storage characteristics. GNFs in this work are synthesized and processed as an additive integrated into LIHCs with an activated carbon-based electrode. Unlike conventional chemical vapor deposition (CVD) methods, which require high temperatures and long reaction times to synthesize graphene sheets, our approach utilizes a cost-effective, microwave plasma-enhanced CVD (PECVD) technique. This method enables the growth of highly conductive GNFs with controlled surface area and 3D architecture at much lower temperatures (<300 °C), using non-toxic gases (organic-catalysis-free) in just 10 minutes. The as-grown GNFs possess good uniformity, high defect density, great conductivity, and good hydrophilicity. With the assistant of GNF, the performance of the LIHC demonstrates a significant enhancement in both capacity and cycle life. The LIHC incorporating 2.5 wt% GNF in electrode presented an impressive capacity of 62.35 mAh g^{-1} at an operating current density of 0.05 A g^{-1}. The champion cell also exhibited moderate cycle stability, retaining 86.4% of its initial capacity after 600 charge/discharge cycles. Additionally, it delivered excellent energy and power densities of 115.58 Wh kg^{-1} and 396.00 W kg^{-1}, respectively. This remarkable performance, particularly in terms of energy density, not only exceeds that of LIHCs employing commercial Super P® as an additive (81.23 Wh kg^{-1}), but also reaches values comparable to the average energy density of lithium-ion batteries.

2. Experimental section

2.1 3D graphene synthesis

A home-made microwave-PECVD system (Fig. S1) was used to synthesize 3D graphene with high efficiency (around 10 min) under a relatively low temperature (<300 °C). The growth temperature was monitored by a non-contact infrared thermometer (RD-3820) with calibrations *via* a digital thermal plate. Based on the same setup we published earlier,[23] modified experimental parameters were applied in this study. Firstly, 1.3 cm by 0.8 cm copper foils (Alfa Aesar, 26 μm thick, purity: 99.996%) were cleaned by an ultrasonic bath with acetone, MeOH, and isopropanol for 10 min each. Dry nitrogen gas was used to remove residual solvents from the copper surfaces gently. Copper foils were then flatted and placed on quartz holders and transferred into a half-inch quartz reaction tube. After flushing with argon (100 SCCM) gas for 20 min, the tube was pumped down to a 1.6×10^{-2} Torr base pressure before starting the following 3D graphene growth. Three mass flow controllers were employed to introduce precise a 10 : 2 : 5 (in SCCM) of $CH_4 : Ar : H_2$ ratio during growth. The microwave plasma source (SAIREM's GMS 200) with an Evenson cavity, which matches the size of the half-inch quartz tube that was equipped as the plasma power source. The Evenson cavity is only 8 mm away from the copper foil, creating an energetic environment for ion bombardment as well as defect formation, which is critical for the porous formation of 3D graphene. The power supply provided an excitation frequency of 2.45 GHz delivering 60 W plasma powers on each sample with a chamber pressure of approximately 0.5 Torr. No active heating was needed during the whole synthesis procedure. After synthesis, dry argon gas was introduced to bring the chamber back to atmospheric pressure. 3D graphene products were collected by gently scraping off the as-grown powder from the copper foil surface for the following slurry preparation to make LIHC electrodes.

2.2 Material characterization

Raman spectroscopy (UniDORN) with 532 nm laser wavelength and an incident power intensity of 20 mW was used to characterize the properties of 3D graphene. The typical acquisition time per spectrum was controlled to be less than 15 seconds to prevent sample burning from the laser. The mapping acquisition was set to be in a 45 μm × 45 μm region with 100 data points collected. The focused ion beam scanning electron microscopy (FIB-SEM) images were taken by an FEI Helios G3CX Compatible system. XPS analysis was carried out with a ULVAC PHI 5000 Versa Probe system, using monochromatic Al K a with a photon energy of 1486.6 eV as the excitation source. The binding energy was calibrated by locating the $4f_{7/2}$ line of clean gold and the $2p_{3/2}$ line of clean copper at 84 eV and 932.67 eV, respectively. The transmission electron microscope (TEM) used was a JEOL JEM-2100F equipped with a Cs Corrector STEM, paired with a ZrO/W (100) Schottky-type electron gun and operated at an accelerating voltage of 200 kV. The resolution was ≤0.23 nm for point resolution and ≤0.1 nm for lattice resolution with the magnification ranged from ×50 to ×1.5 million.

2.3 Preparation of AC/LFP electrodes and coin Cell-LIHCs assembly

In this study, activated carbon (AC) was used as the anode material, while a mixture of AC (ACS20, CSCC) and $LiFePO_4$ (LFP, UBIQ Tech.) was used as the cathode material in a weight ratio of 6.6 : 1. Several conductive additives, GNFs (0.8 wt%, 2.5 wt%, 5.0 wt%, 7.5 wt%) and commercial Super P (5.0 wt%, 10.0 wt%, UBIQ Tech.) were separately doped into the cathode for comparison. Polyvinylidene difluoride (PVDF, Solef 5130, SOLVAY) was used as the binder to prepare the LIHC composite electrode. First, before mixing, NMP (≥99.9%, ULVAC) and PVDF were stirred at 750 rpm for more than 24 hours until they were fully dissolved and appear clear and transparent. Next, the active materials and additives powder were grinded in an agate mortar and mixed in the PVDF blend and stirred at 750 rpm for another 24 hours. The as-prepared slurry was then coated onto aluminium foil and dried in an oven at 60 °C for 24 hours to completely remove NMP. Finally, the electrodes were cut into circular button-shaped electrodes with a diameter of 13 mm, matching the required size for CR2032 LIHC coin cell. The dried electrodes were stored in an oven at 60 °C to effectively prevent direct exposure to the atmosphere. Each LIHC coin cell consists of asymmetric current collectors and a layered electrode structure, with a circular separator membrane (15 mm in diameter, pre-soaked in electrolyte) placed in between, and 45 μL of organic electrolyte containing lithium hexafluorophosphate ($LiPF_6$, in EC/EMC/DMC in 1 : 1 : 1wt%, ULVAC) as the electrolyte. The components were assembled in an argon-filled glove box (SG/LG, Vigor) with O_2 and H_2O levels below 0.05 ppm.

2.4 Electrochemical measurements

In two-electrode system, Cyclic Voltammetry (CV) spectra were collected using the Bio-Logic SP-150 electrochemical workstation with voltage range from 0.1 to 3.8 V under a 50 mV s^{-1} scan rate. Electrochemical impedance spectroscopy (EIS) measurements were carried out using a frequency response analyzer (also Bio-Logic SP-150) where the EIS spectra were measured in the frequency range of 10 mHz to100 kHz under a 10 mV_{rms} voltage amplitude. In the capacities test, a Galvanostatic charge/discharge tester (GC/D, BTS-5V50 mA) was employed under constant current condition with a voltage ranging from 0.1 to 3.8 V. All the capacities, energy density, and power density in this research were calculated by using the data obtained from the GC/D curve after subtracting the IR drop. For each experimental recipe, a minimum of five coin-cells were fabricated and analyzed, ensuring a capacity deviation of less than 1%.

3. Results and discussion

3.1 Material characterization of PECVD-grown 3D graphene

The as-synthesized 3D graphene was firstly analyzed using Raman spectroscopy to assess its quality and structural characteristics. As shown in the single-point Raman spectrum in Fig. 1a, three major graphene bands were observed: the D band at 1350 cm^{-1}, the G band at 1580 cm^{-1}, and the 2D band at 2700 cm^{-1}. The 2D-to-G ratio confirms that the 3D graphene exhibits a multi-layer structure, with boundary-type defects indicated by the presence of the D′ shoulder around 1620 cm^{-1}.[24,25] Additionally, the optical microscope image in Fig. S2 reveals a uniform graphene coating on the Cu foil surface. Spatial Raman mapping of the I_D/I_G ratio (Fig. 1b) and the I_{2D}/I_G ratio (Fig. S3) further confirm its uniformity and indicate that the as-grown graphene-based material has a high defect density and consists of a few graphene layers. This structural composition suggests its potential for benefiting both capacity and conductivity in LIHCs. To further examine the chemical bonding in the as-grown graphene, X-ray photoelectron spectroscopy (XPS) was conducted, and the detailed carbon 1s spectrum is shown in Fig. 1c. The fitting curves show that the as-grown graphene is mainly composed of C=C(sp^2), C–C(sp^3), C–OH, and π–π* interactions.[26] As shown in Table S1, the material primarily consists of sp^2-hybridized graphene, with C=C(sp^2) and C–C(sp^3) comprising 54.91% and 18.91%, respectively. This high crystallinity indicates minimal disruption of sp^2 bonds, with limited formation of sp^3 or C–OH bonds, which can be considered defects that provide additional sites for ion storage in LIHCs. The presence of C–OH bonds could also enhance the material's hydrophilicity, while π–π* interactions improve electrical conductivity and structural stability. Owing to our customized gas flow conditions during synthesis, trace oxygen functional groups were allowed to be introduced into the graphene. Contact angle measurements on the graphene product on a copper foil substrate was conducted and supports this conjecture. The results in Fig. 1d show that the contact angle of the as-grown graphene is 88.54° (<90°), indicating slight hydrophilicity, which differs from the hydrophobic nature of typical multilayer graphene. Since the $LiPF_6$ solution in a typical battery electrolyte (EC/DMC) is polar, the hydrophilic surface of the as-synthesized material may facilitate better interaction between them. To gain a better understanding of the surface morphology of the as-synthesized graphene and to assess its microscopic structure, a scanning electron microscopy (SEM) study was then performed. As shown in Fig. 1e, the sample surface exhibits a continuous and wrinkled structure with numerous edges. Furthermore, the high-magnification image in Fig. 1f reveals abundant fine branches within the material's layered structure. These branches along with defects could provide a large number of electron/ion adsorption sites for capacitors. The synthesis parameters were further refined, assisted by focused ion beam (FIB) imaging, to maximized 3D graphene's functionality for hybrid capacitor integration. Further details on the 3D graphene synthesis are provided in the Experimental Section, adapted and modified from our earlier publication.[23]

FIB images of PECVD-grown 3D graphene under two different argon conditions (Ar-rich and Ar-low) were firstly analyzed, as shown in Fig. 2a and b, respectively. It is reported that the growth mechanism of vertical graphene sheets is governed by the competition between carbon deposition and etching.[27] The top-view images (left panels) of Fig. 2 clearly

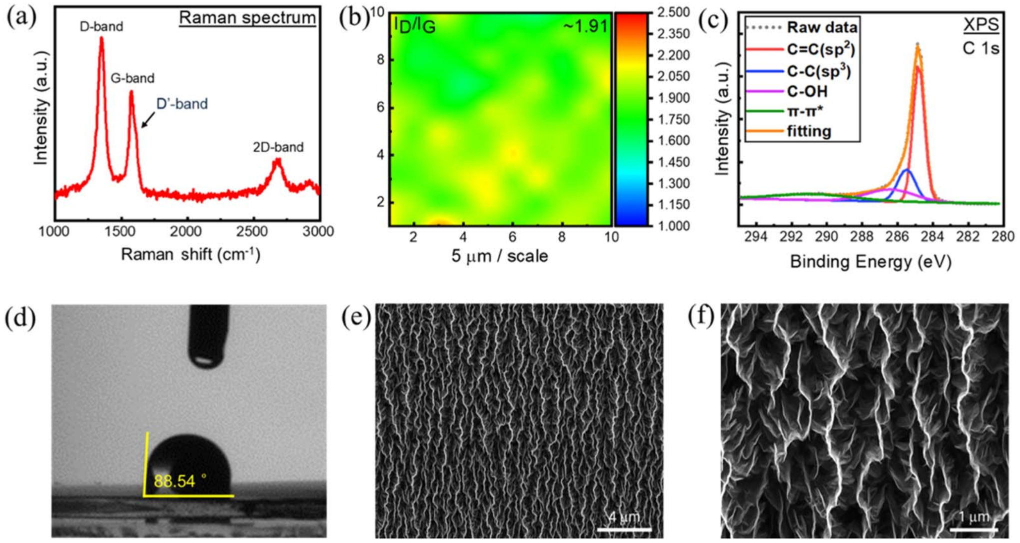

Fig. 1 (a) Raman spectrum of the as-synthesized graphene. (b) Spatial Raman mapping of the I_D/I_G ratio with a mean value of about 1.91. (c) XPS spectrum of carbon 1s with both raw data and fitted curves. (d) Contact angle study on the graphene surface. (e) SEM image of the as-synthesized 3D graphene on copper foil. (f) Magnified SEM image to display 3D structure.

indicate that the lower Ar concentration results in a significantly higher graphene density. Additionally, the cross-sectional views (right panels) reveal a notable increase in branch density when the partial pressure of argon is reduced. High concentrations of Ar could effectively suppress the carbon etching process by H_2—produced from the decomposition of CH_4—leading to significantly weaker etching and fewer branch formations. For hybrid capacitor applications, the denser 3D graphene structure in Fig. 2b is preferred due to its abundance of ion storage sites. Nevertheless, the product with high density may hinder ion intercalations since the spacing between stripes could be partially closed. As a result, to optimize both spacing and specific surface area—enhancing the capacity of LIHCs—additional H_2 was introduced to selectively thin the graphene edges, as illustrated schematically in Fig. 3c. The additional H_2 could further enhance the etching rate at the boundaries, leading to thinner stripe and even higher branch density. The FIB image of the optimized 3D graphene material, grown with a $CH_4 : Ar : H_2$ ratio of 10 : 2 : 5, is presented in Fig. 2d. Comparing Fig. 2b and d, it is evident that the stripe margins were significantly reduced while maintaining a high branch density, exceeding that of Fig. 2a. It is worth noting that the orientation of the vertically

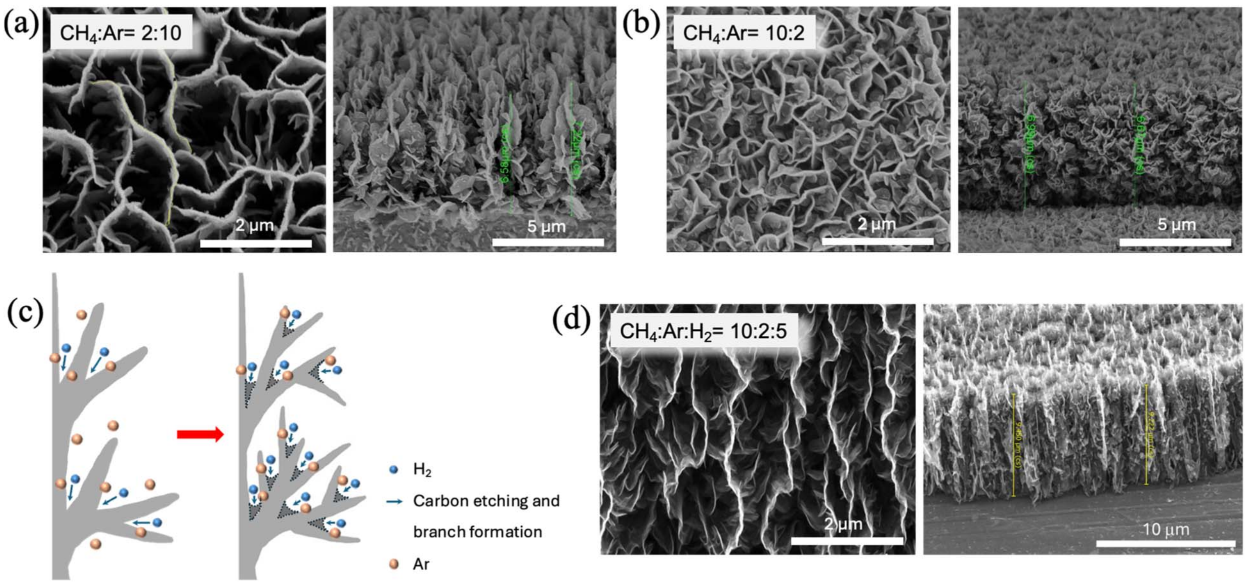

Fig. 2 (a) FIB images of PECVD-grown 3D graphene under Ar-rich condition with cross-sectional view on the right panel. (b) Image of 3D graphene with low argon growth condition. (c) Schematic of the 3D graphene growth mechanism with additional H_2 introduced. (d) FIB image of the optimized 3D graphene, grown with a $CH_4 : Ar : H_2$ ratio of 10 : 2 : 5.

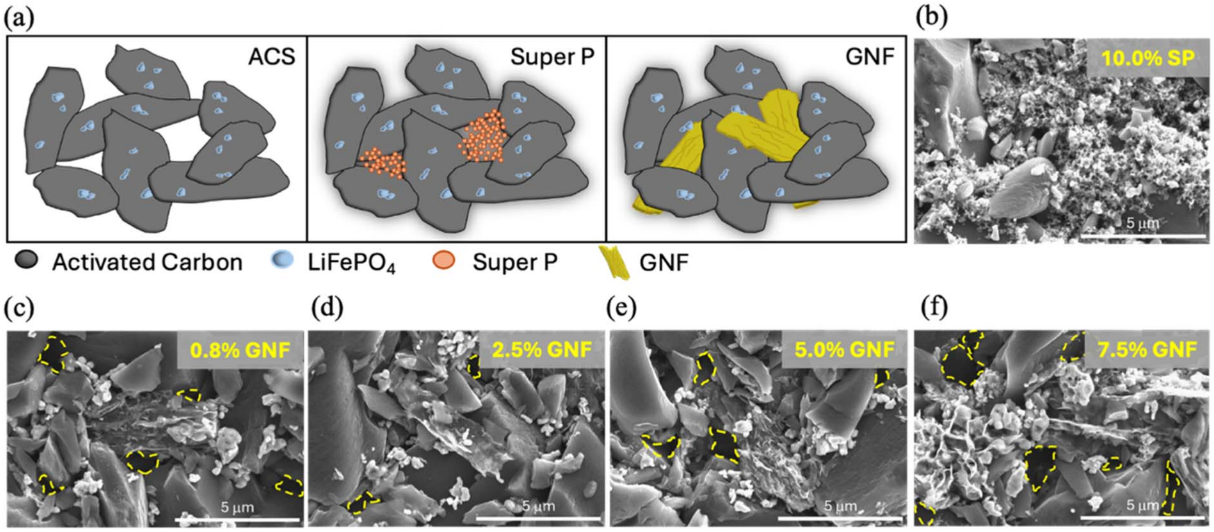

Fig. 3 (a) The schematic sketch of activated carbon-based electrode with Super P and GNF additives. (b) FIB image of the electrode mixing activated carbon with 10.0% Super P conductive additive. (c) FIB images of the electrode with 0.8 wt%, (d) 2.5 wt%, (e) 5.0 wt%, and (f) 7.5 wt% GNF conductive additive.

grown 3D graphene should not play a critical role, as the material (grown in 10 minutes) will be harvested from the copper foil and processed further before being incorporated into the electrode slurry. Additionally, the cross-sectional image of the optimized material shown in the right panel of Fig. 2d reveals a thin, dense 3D architecture with great potential for securing ions and charge carriers. From the side-view image, the branches exhibit a dense yet uniform structure without noticeable aggregations. This characteristic is crucial for extending the carrier migration path within electrodes, reducing internal resistance, preventing cluster formation, and ultimately enhancing ion intercalation efficiency for capacitors. Details of the 3D graphene structure, such as interlayer spacing, number of layers, and estimated specific surface area (SSA), were further analyzed using TEM images, as shown in Fig. S4. The interlayer spacing of 3D graphene grown under a high Ar flow condition was measured to be 0.353 nm using ImageJ software, whereas that grown under a low Ar flow condition exhibited a spacing of 0.338 nm, corresponding to Fig. S4a and b, respectively. Both values are greater than the typical interlayer spacing of graphite, which is 0.335 nm.[28,29] Furthermore, based on the edge-on TEM images, the number of layers in the 3D graphene grown under high Ar flow (9 layers) and low Ar flow (7 layers) conditions were both observed to be fewer than 10, consistent with the general definition of graphene.[30,31] Knowing the number of graphene layers allows us to estimate the material's specific surface area.[32] Given that monolayer graphene has an SSA of 2630 $m^2\ g^{-1}$, the SSA can be estimated using the equation: $SSA = 2630/N\ (m^2\ g^{-1})$, where N is the number of graphene layers. For the high Ar condition (9 layers), the SSA is approximately 292.2 $m^2\ g^{-1}$, while for the low Ar condition (7 layers), the SSA is approximately 375.7 $m^2\ g^{-1}$. Also, according to BET and BJH analyses, the average pore size is approximately 21.4 nm, falling within the mesoporous range (a few to ∼40 nm), and the pore volume is about 0.52 $cm^3\ g^{-1}$, as displayed in Table S2. Since the TEM sample was prepared by ultrasonically dispersing the graphene powder in ethanol and then drop-casting the suspension onto a copper grid, the clear image of the graphene layered structure suggests the robustness and stability of the synthesized graphene. The 3D graphene grown using the optimized recipe was then introduced into the electrode slurry, and a high-resolution FIB analysis was conducted to gain deeper insights into different mixing conditions as well as designate the optimal scenario.

3.2 Investigation of electrodes with Super-P and 3D graphene

LIHC electrodes with SP and 3D graphene as conductive additives in various ratios were carefully studied through FIB imaging. It should first be noted that the 3D graphene harvested from copper foil after processing (see Experimental section) exhibited a more flake-like structure with branches. When introduced into the slurry and coated onto the electrode, it adopts an arbitrary orientation, differing from the vertically aligned, continuously extended structure with a high aspect ratio observed right after synthesis in Fig. 2. This thin, flexible, and small fragment-like structure of graphene nanoflakes is expected to be beneficial for three-dimensionally intercalating the gaps or voids between activated carbon clusters. The conjectured scenarios of activated carbon with Super P (SP) and GNF additives are proposed and illustrated in the schematic sketch in Fig. 3a. For the case of ACS (activated carbon) and $LiFePO_4$ without any conductive additives (left panel), large gaps exist between carbon clusters, potentially reducing the electrode's conductivity. When SP is added (middle panel), it helps fill these gaps and form a denser structure. However, due to extended electron transport networks while rearranging the spacing between them.

The conjectures were supported by the high-resolution FIB studies with images displayed in Fig. 3b–f. In the undoped electrode (Fig. S5), many large voids can be observed between the activated carbon materials. These voids are caused by the relatively large particle size of the activated carbon with irregular structure, which lead to the formation of numerous vacancies. In Fig. S6, 5.0 wt% of SP effectively fills these voids, facilitating the formation of more intimate structure for electron transport. After doping with 10.0 wt% of SP in Fig. 3b, the electrode's surface morphology changed even more notably compared to the electrode with 5.0 wt% of SP. However, when the doping ratio rose to 10.0 wt% (Fig. 3b), a large portion of the active material surface becomes covered, making it difficult for the electrolyte to penetrate. Additionally, due to the solid spherical structure of SP, it does not provide a high specific surface area to replace activated carbon for ions storage. On the other hand, the electrodes cooperated with GNF were analyzed in Fig. 3c–f with various doping ratios. In Fig. 3c, the image of the electrode is primarily composed of ACS and $LiFePO_4$, with only a small amount of GNF (0.8 wt%) interspersed among them. Numerous voids can still be observed between the ACS clusters (highlighted in yellow), as the amount of graphene flakes is insufficient to completely fill these gaps. As the GNF concentration rose to 2.5 wt% in Fig. 3d, the 3D flakes were more intimately inserted between ACS particles, filling voids and three-dimensionally conjoining the activated carbon with a flexible, thin, and stretched structure. Furthermore, the insertion of GNF between the active materials increased interlayer spacing, prevented activated carbon agglomeration, enhanced the specific surface area for reactions, and reduced internal resistance.

The doping concentration is optimally balanced to fit into the complex structure with minimal voids while avoiding excessive coverage of the activated carbon surface. When the doping concentration reached 5.0 wt% (Fig. 3e), most of the vacancy defects were filled but slight aggregation and curling of the GNF itself could be observed. Although the structure of GNF can still provide electron storage sites, aggregation may cause excessive structural compression, preventing GNF from fully expanding in 3D and utilizing its structural advantages. This could lead to an increase in internal resistance rather than a reduction. In addition, the excessive intercalation of GNF between active materials results in a squeezing effect, which in turn creates new vacancy defects as circled in yellow dashed courses. As a result, more visible voids appear between layers compared to Fig. 3d. With a further increase to 7.5 wt% GNF in Fig. 3f, the aggregation became even more severe, leading to larger vacancies. This may prevent GNF from providing effective charge transport networks, significantly increasing the internal resistance of the electrode and consequently reducing the cell's capacity as well as the cycling stability.

3.3 Electrochemical characterizations of LIHCs with GNF cooperated

A series of electrochemical tests were then conducted on LIHC coin cells with commercial additive and GNFs with various doping ratios. These tests included EIS, CV, G/CD cycling tests, high current tests, and cycle life tests (600 cycles). First, Fig. 4a illustrates the internal working principle of the LIHC in this study. During charging/discharging, lithium ions are extracted/absorbed while positive and negative charges form a double-layer structure at both electrodes. At the cathode, Li^+ ions are intercalated into or deintercalated from the crystal structure, undergoing faradaic reactions involving charge transfer processes. On the counter electrode, the working principle relies on pure physical adsorption (electrostatic), without ion intercalation or redox reactions, resulting in a fast and highly reversible process that delivers high power density. The hybrid cell based on two different energy storage mechanisms allows for outstanding capacity while maintaining a decent charge–discharge speed. It is important to note that the field of lithium-ion hybrid capacitors encompasses a variety of mechanisms and configurations, as it combines diverse energy storage principles and materials. In this work, the LIHC is inspired and modified based on established concepts reported in recent literature.[9] The Nyquist plots displayed in Fig. 4b and c based on the EIS measurement reveal more impedance characteristics of the LIHC such as interfacial properties, charge transfer resistances, and reaction mechanisms.[33] The impedance analysis was performed after activating the sample with three charge–discharge cycles at a current density of 0.05 A g^{-1} and the resulting data curves were fitted using an equivalent circuit model in Fig. S7 with corresponding equivalent series resistance (ESR) and charge transfer resistance (R_{ct}).[34] As shown in Fig. 4b, the coin cell without any doping additives exhibited the highest ESR (largest semicircle diameter), indicating the highest internal resistance of the material. However, after adding 5 wt% of Super P, the ESR significantly decreased, demonstrating its effective role in mitigating vacancy defects. While testing different doping ratios of GNF, Fig. 4c shows that a doping level of 2.5 wt% resulted in the best performance in terms of both ESR and R_{ct}, suggesting an overall decline of both internal resistance and the contact resistance (between the electrode and the electrolyte). This improvement signifies great charge transfer efficiency in LIHC which could subsequently boosts device performance. These findings align well with material analysis in Fig. 1 and 2, and the electrode studies in Fig. 3. All the resistances from the EIS tests were calculated and summarized in Table S3. Next, CV test was conducted to characterize the charge/discharge processes by a scan rate of 1 mV s^{-1}.[35] As shown in Fig. 4d, the optimal doping ratio in the GNF doping measurement was determined to be 2.5 wt%, which exhibited the highest capacity, followed by 5.0 wt%, 0.8 wt%, and 7.5 wt%. The samples for each ratio demonstrated complete and stable cycling, indicating a stable internal current cycle. Furthermore, when the scan rate was increased to 5 mV s^{-1} and 10 mV s^{-1} (Fig. 4e), the LIHC coin cell with 2.5 wt% GNF added maintained high stability, with smooth curves and no noticeable deformation. Besides, as shown in Fig. 4f, the cell with 2.5 wt% GNF exhibited a significantly larger cyclic area, indicating a much higher capacity compared to the one with 5.0 wt% commercial conductive additive (Super P). This result can likely be attributed to the well-formed 3D interconnected

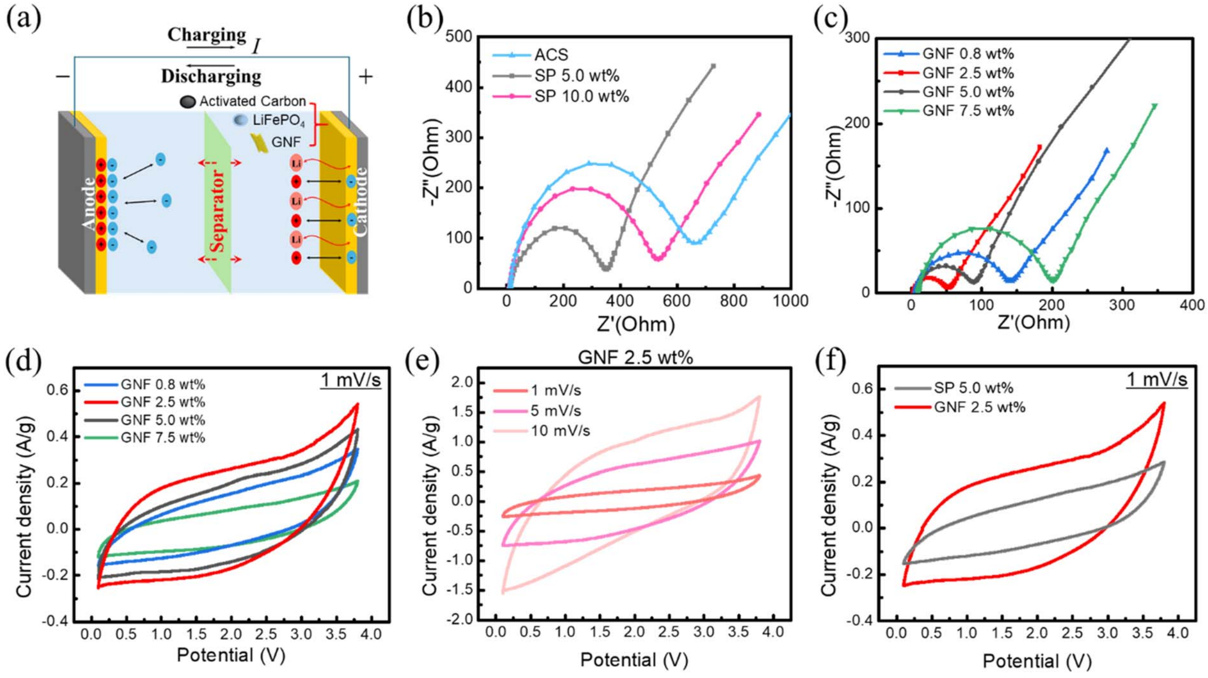

Fig. 4 (a) Internal reaction mechanism of LIHC during charging and discharging with both physical adsorption–desorption reaction and electrochemical Faraday reaction. (b) The Nyquist plots of the EIS measurements reveal the impedance characteristics of the LIHCs with and without SP as the conductive additive. (c) The Nyquist plots of the LIHCs with GNF as the conductive additive in different ratios. (d) CV test of the LIHCs with GNF in different ratios by a scan rate of 1 mV s^{-1} (e) CV test of the LIHCs with GNF by increased scan rate to 5 mV s^{-1} and 10 mV s^{-1}. (f) Direct comparison of CV curves between the best GNF and SP cells.

AC clusters, enriched with abundant ion storage sites provided by the graphene branches, as illustrated in Fig. 3. This superior performance highlights the advantage of GNF over SP as a conductive additive in LIHCs. Notably, this is the first study to demonstrate impressive overall performance of LIHCs by utilizing PECVD-synthesized 3D graphene as a conductive additive. An approximate estimation of specific capacity was obtained by integrating the CV curves. The resulting capacities were 224.4 mAh g^{-1} and 449.7 mAh g^{-1} for the best-performing LIHCs incorporating SP and GNF, respectively. However, due to factors such as scan rate dependency, the coexistence of faradaic and non-faradaic (capacitive) currents, and potential contributions from side reactions, these values are considered indicative of relative performance rather than absolute capacity. A more accurate quantification will be presented and discussed in the subsequent galvanostatic charge/discharge analysis.

Additional GC/D tests were carried out to further analyze the electrochemical properties of LIHCs with different additives and ratios. It should be mentioned that due to the dual functionalities of hybrid capacitors, both specific capacity (mAh g^{-1}) and specific capacitance (in F g^{-1}) are commonly used to quantify energy storage capability. In this study, specific capacity was selected, as the charge storage performance is higher than that of typical supercapacitors and approaches the level of lithium-ion batteries. As shown in Fig. 5a, the test results indicate that the hybrid capacitor without any additives had a specific capacity of 32.46 mAh g^{-1}. When doped with 5 wt% SP, the specific capacity increased to 43.91 mAh g^{-1}, but further increasing the SP content to 10 wt% reduced the specific capacity to 34.19 mAh g^{-1}. The optimal performance of 5 wt% SP is attributed to its ability to effectively fill vacancy defects without excessively covering the activated carbon surface as revealed in Fig. 3. In Fig. 5b, among the different GNF doping ratios, 2.5 wt% demonstrated the best performance, achieving a discharge specific capacity of 62.35 mAh g^{-1}, outperforming all tested groups. Based on the structural analysis using FIB in Fig. 3 as well as the electrical properties observed from EIS in Fig. 4b and c, GNF doping could adjust the active material structure within the electrode more properly, enhancing charge transfer and energy storage capabilities. As a result, a more complete discharge curve along with a smaller IR drop were observed when comparing the GC/D data in Fig. 5a and b. In this study, the initially fabricated LIHCs exhibited high coulombic efficiency of nearly 100% with a smaller operation window (∼2 V). However, after adjusting the ratio of lithium iron phosphate in the electrode (ACS : LFP = 6.6 : 1), we observed that the charge–discharge voltage range could be extended considerably. Remarkably, the GC/D curves maintained smooth and regular charge–discharge profiles even under the extended voltage window. This behavior may be ascribed to a characteristic inherited from supercapacitors, the ability to tolerate discharge down to almost 0 V. Consequently, we broadened the voltage range to explore the operational limits. Although this adjustment resulted in a moderate decrease in coulombic efficiency to a decent level of approximately 90% (GNF 2.5 wt%), it led to a substantial enhancement

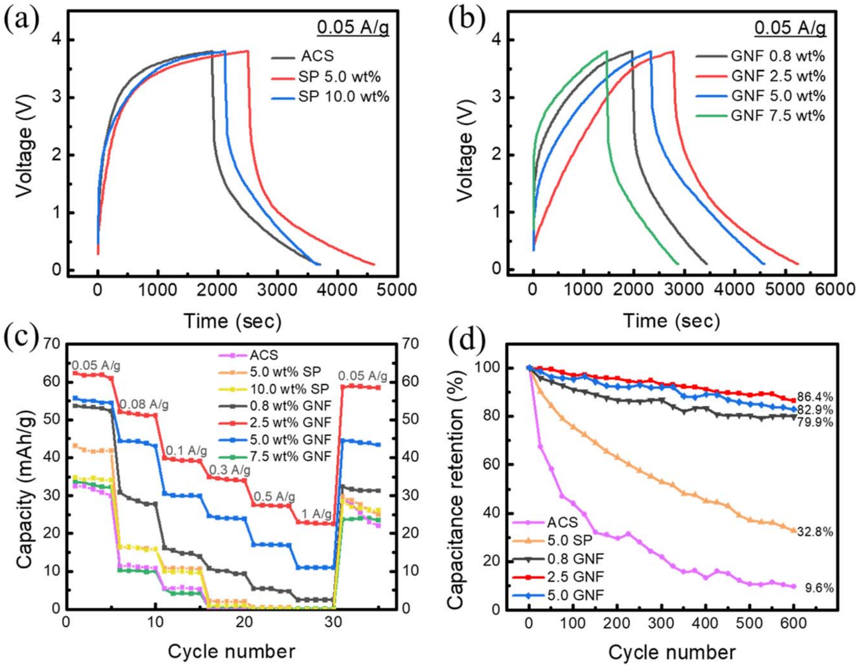

Fig. 5 (a) The GC/D tests of hybrid capacitors without and with SP as the conductive additive. (b) The GC/D measurements of LIHCs with GNF as the additive with various ratios. (c) Rate performance at current densities from 0.05 A g^{-1} to 1 A g^{-1} with various doping conditions. (d) The long-term cycling test with a fixed current density of 0.05 A g^{-1} for 600 cycles on electrodes with different doping ratios.

in energy density—exceeding that of most supercapacitors and approaching the performance of lithium-ion batteries. These findings demonstrate the potential advantage of hybrid capacitors in combining the strengths of both energy storage technologies. Besides, Fig. 5c shows that electrodes without dopants, as well as those doped with 5 wt% and 10 wt% SP, fail to respond at high currents. When the current density exceeds 0.3 A g^{-1}, their capacity drops to nearly zero, indicating that these doping ratios cannot stably provide ion transport channels within the electrode under high current density conditions. In contrast, electrodes doped with 2.5 wt% and 5.0 wt% GNF remained functional even at operating currents as high as 1 A g^{-1}. Moreover, the 2.5 wt% GNF-doped electrode demonstrated the best performance, maintaining a discharge specific capacity of 23.05 mAh g^{-1} at 1 A g^{-1} with a capacity retention rate of 93.87%, significantly surpassing the performance of the 5.0 wt% GNF and 10.0 wt% SP cells. At higher current densities, lithium ions intercalate into the electrodes more rapidly, causing the material to expand and shrink quickly, which leads to mechanical damage as well as capacity degradation. Due to its high robustness and mechanical strength, GNF is expected to provide excellent support and buffering between active materials under high-current conditions, effectively reducing structural deformation of electrodes. Finally, a long-term cycling test was performed with a fixed current density of 0.05 A g^{-1} for 600 cycles on electrodes with various doping ratios. As shown in Fig. 5d, the stability of the LIHCs doped with 3D graphene improved remarkably. The best-performing device, with 2.5 wt% GNF, maintained 86.4% of its initial capacity after 600 cycles, demonstrating relatively better cycling performance. In contrast, the electrode with 5.0 wt% SP additive retained only 32.8% of its capacity, while the undoped electrode maintained a mere 9.6%. These results clearly indicate that GNF effectively mitigates specific capacity degradation, possibly by providing lower internal resistance as well as more stable and robust structural support for the electrode. The FIB analysis after 600 cycles was conducted on the same LIHC by disassembling the coin cell. Fig. S8 shows the FIB image of the electrode after 600 cycles, indicating that although some 3D graphene flakes remained visible, they were apparently compressed and gradually lost their 3D structure. This structural degradation may lead to the overall retention performance of the GNF-added LIHCs being moderate rather than excellent, as compared with relevant reports. Considering the aggressive operating conditions with a large voltage window applied in this study, the retention performance is expected to be much better under a smaller voltage window.

3.4 Comparison with existing studies

Finally, a Ragone plot was made to compare the energy density and power density of the optimized 2.5 wt% GNF-doped LIHC device in this study with existing literature. In the field of hybrid capacitors, different research teams may use different structures, materials, and specific capacity/capacitance units. Converting data into a Ragone plot enables direct and reasonable comparison of energy and power densities across storage devices, allowing efficient assessment of their advantages and characteristics.[36] In this study, energy density was measured using the Galvanostatic charge–discharge tester, and power density was calculated accordingly through the basic unit conversion equation between power and energy:

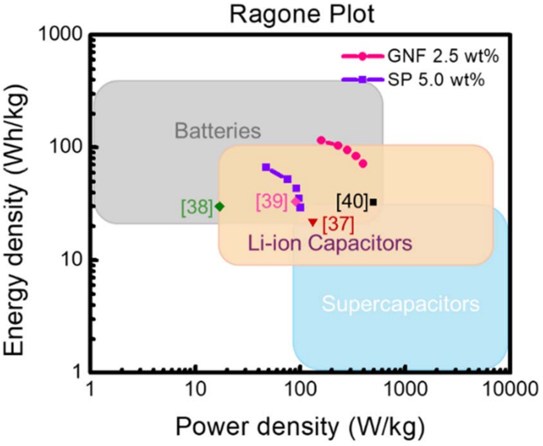

Fig. 6 The Ragone plot comparing the energy density and power density of the optimized 2.5 wt% GNF-doped LIHC and 5.0 wt% SP doped device in this study with existing literature.

$$P_{\text{density (W kg}^{-1})} = E_{\text{density (Wh kg}^{-1})}/\Delta t \times 3600 \qquad (1)$$

where Δt is the discharge time in seconds. Details of the conversion from specific capacity to energy density can also be found in the SI. The results in Fig. 6 show that in an assembled LIHC coin cell, the 2.5 wt% GNF-doped device achieved a maximum energy density of 115.58 Wh kg^{-1} and a maximum power density of 396.00 W kg^{-1}. In comparison, the 5.0 wt% SP-doped device had a maximum energy density of 66.53 Wh kg^{-1} and a power density of 100.11 W kg^{-1}. These results suggest that the GNF-assisted approach in this study successfully improves the device's internal resistance, contact area, resulting in much better electrode characteristics and device performance. The champion cell, integrated with the proposed material and fabrication process, significantly advances both energy and power density in lithium-ion hybrid capacitors. To the best of our knowledge, as shown in Fig. 6, the performance surpasses most existing reported LIHCs utilizing either commercial or custom-designed electrode materials with similar architectures.[37–40] The approach we proposed in this work provides a valuable and practical strategy for the development of high-performance energy storage devices suitable for various commercial applications.

Although the best-performing LIHC in this study has achieved remarkable performances, we are continuing to optimize the capacity matching by employing a three-electrode system, which enables real-time monitoring of the potentials at both the positive and negative electrodes during the GC/D process. Building on the promising materials and methodology presented in this work, we anticipate the development of a next-generation LIHC with an even better energy density, or integration with other types of hybrid devices, such as zinc-ion hybrid capacitors.[41,42]

4. Conclusions

In this work, 3D graphene nanoflakes were synthesized through an efficient and eco-friendly method and used as an additive in LIHCs. Unlike traditional CVD techniques, our approach allows GNF synthesis at significantly lower temperatures (<300 °C) in just 10 minutes, without the use of toxic gases (organic-catalysis-free). With the addition of GNFs as conductive additive in various doping ratios, the LIHC demonstrated remarkable improvements in both capacity and cycle life. The LIHC incorporating 2.5 wt% GNF in electrode achieved an impressive specific capacity of 62.35 mAh g^{-1} at an operating current density of 0.05 A g^{-1}. The best cell also exhibited outstanding cycle stability, retaining 86.4% of its initial capacity after 600 charge/discharge cycles. Moreover, it delivered excellent energy and power densities of 115.58 Wh kg^{-1} and 396.00 W kg^{-1}, respectively. These results not only exceed the specific capacity of LIHCs using commercial Super P® (43.91 mAh g^{-1}) but also surpass most existing records with similar cell architectures and electrode materials. This work provides an efficient and clean approach for synthesizing promising 3D graphene for the development of high-performance LIHCs and other energy storage devices.

Author contributions

Yu-Han Chou: data curation (lead), formal analysis (lead), methodology (equal); Wan-Ying Wu: formal analysis (TEM); Jai-De Wei: formal analysis (contact angle); Ting-Wei Wu: data curation (cell disassembly); Wei-Shiuan Tseng: writing – original draft, conceptualization (lead), data curation (equal), formal analysis (equal), funding acquisition (lead), investigation (lead), methodology (lead), supervision (lead), writing – review & editing (lead).

Conflicts of interest

There are no conflicts to declare.

Data availability

The data supporting this article has been included as part of the supplementary information (SI). Supplementary information: the home-made PECVD system (Fig. S1), optical microscope image of 3D graphene (Fig. S2), Spatial Raman mapping of the I2D/IG ratio (Fig. S3), TEM image of 3D graphene (Fig. S4), FIB image of pure electrode (ACS and LFP) without conductive additive (Fig. S5), FIB image of the electrode mixing activated carbon with 5.0% Super P (Fig. S6), equivalent circuit of the LIHC (Fig. S7), post-mortem analysis (Fig. S8), XPS bond component of the as-synthesized 3D graphene (Table S1), pore volume analysis of GNF (Table S2), and resistances calculated from the EIS tests (Table S3). See DOI: https://doi.org/10.1039/d5ra06831b.

Acknowledgements

This work was supported by the Higher Education Sprout Project of the National Yang-Ming Chiao-Tung University and Ministry of Education (MOE), Taiwan. Ministry of Science and Technology (MOST), Taiwan (MOST 110-2112-M-A49-028-MY2);

National Science and Technology Council (NSTC), Taiwan (NSTC 112-2112-M-A49-023, NSTC 113-2112-M-A49-009, and NSTC 114-2112-M-A49-002).

References

1 A. Burke, *J. Power Sources*, 2000, **91**, 37–50.
2 J. Wu, L. Hu, Z. Hu, W. Yi, Z. Mu, J. Zhang, Y. He, J. Liu and C. Fan, *Nanoscale*, 2025, **17**, 17334–17344.
3 A. Tomar, N. Choudhary, R. Jain, D. Chaudhary, G. Malik, S. Issar and R. Chandra, *Nanoscale*, 2025, **17**, 16457–16475.
4 Z. Zhai, L. Zhang, T. Du, B. Ren, Y. Xu, S. Wang, J. Miao and Z. Liu, *Mater. Des.*, 2022, **221**, 111017.
5 D. Meena, R. Kumar, S. Gupta, O. Khan, D. Gupta and M. Singh, *J. Energy Storage*, 2023, **72**, 109323.
6 D. Gao, Z. Luo, C. Liu and S. Fan, *Green Energy Environ.*, 2023, **8**, 972–988.
7 A. Chu, *J. Power Sources*, 2002, **112**, 236–246.
8 J. Söderbom, *European Institute of Innovation and Technology*, 2020, pp. 1−36.
9 N. W. K. Wan, H. N. Lim, I. Ibrahim, N. M. Huang, C. Y. Foo and Z. T. Kiang, *Chem. Eng. J.*, 2023, **456**, 141132.
10 M. W. Verbrugge, P. Liu and S. Soukiazian, *J. Power Sources*, 2005, **141**, 369–385.
11 Z. Chen, Q. Zhang and Q. Liang, *Nanomaterials*, 2022, **12**, 1936.
12 M. R. Lukatskaya, B. Dunn and Y. Gogotsi, *Nat. Commun.*, 2016, **7**, 12647.
13 M. Beg, K. M. Alcock, A. T. Mavelil, D. O'Rourke, D. Sun, K. Goh, L. Manjakkal and H. Yu, *ACS Appl. Mater. Interfaces*, 2023, **15**, 51100–51109.
14 A. D. Jara, A. Betemariam, G. Woldetinsae and J. Y. Kim, *Int. J. Min. Sci.*, 2019, **29**, 671–689.
15 U. Kydyrbayeva, Y. Baltash, O. Mukhan, A. Nurpeissova, S.-S. Kim, Z. Bakenov and A. Mukanova, *J. Energy Storage*, 2024, **96**, 112629.
16 M. N. Norizan, M. H. Moklis, S. Z. N. Demon, N. A. Halim, A. Samsuri, I. S. Mohamad, V. F. Knight and N. Abdullah, *RSC Adv.*, 2020, **10**, 43704–43732.
17 K. Phothong, C. Tangsathitkulchai and P. Lawtae, *Molecules*, 2021, **26**, 5641.
18 A. K. Geim, *Science*, 2009, **324**, 1530–1534.
19 K. M. Liao, Y. K. Dai, H. U. Wang, S. Deng and G. P. Dai, *ACS Appl. Energy Mater.*, 2025, **8**, 3892–3903.
20 Y. Kumar, G. Koyyada, T. Ramachandran, J. H. Kim, S. Sajid, M. Moniruzzaman, S. Alzahmi and I. M. Obaidat, *Nanomaterials*, 2023, **13**, 1049.
21 H. U. Wang, Y. K. Dai, K. M. Liao, S. Deng and G. P. Dai, *J. Phys. Chem. Lett.*, 2025, **16**, 1103–1113.
22 T. B. Lv, Y. K. Dai, L. Tan, J. J. Zhang, Z. Q. Zhao, K. M. Liao, H. Y. Wang, S. Deng and G. P. Dai, *ACS Appl. Nano Mater.*, 2024, **7**, 24346–24355.
23 W. S. Tseng, F. S. Tseng, H. W. Lai, W. Y. Wu and M. Y. Chen, *J. Sci.: Adv. Mater. Devices*, 2023, **8**, 100605.
24 M. F. Abdullah and N. J. N. B. Nazim, *Mater. Lett.*, 2022, **308B**, 131274.
25 F. Al-Hazmi, G. W. Beall, A. Al-Ghamdi, A. Alshahrie, F. Shokr and W. E. Mahmoud, *J. Mol. Struct.*, 2016, **1118**, 275–278.
26 X. Chen, X. Wang and D. Fang, *Fullerenes, Nanotubes Carbon Nanostruct.*, 2020, **28**, 1048–1058.
27 S. Ghosh, K. Ganesan, S. R. Polaki, S. Ilango, S. Amirthapandian, S. Dhara, M. Kamruddin and A. K. Tyagi, *RSC Adv.*, 2015, **5**, 91922–91931.
28 L. Zhang, Z. Sun, J. L. Qi, J. Shi, T. Hao and J. Feng, *Carbon*, 2016, **103**, 339–345.
29 M. Winter, B. Barnett and K. Xu, *Chem. Rev.*, 2018, **118**, 11433–11456.
30 A. K. Geim and K. S. Novoselov, *Nat. Mater.*, 2007, **6**, 183–191.
31 A. Bianco, H.-M. Cheng, T. Enoki, Y. Gogotsi, R. H. Hurt, N. Koratkar, T. Kyotani, M. Monthioux, C. R. Park and J. M. Tascon, *Carbon*, 2013, **65**, 1–6.
32 S. Marchesini, P. Turner, K. R. Paton, B. P. Reed, B. Brennan, K. Koziol and A. J. Pollard, *Carbon*, 2020, **167**, 585–595.
33 A. Amirudin and D. Thieny, *Prog. Org. Coat.*, 1995, **26**, 1–28.
34 K. K. Kar, *Handbook of Nanocomposite Supercapacitor Materials II*, Springer, 2020.
35 X. Huang, Z. Wang, R. Knibbe, B. Luo, S. A. Ahad, D. Sun and L. Wang, *Energy Technol.*, 2019, **7**, 1801001.
36 E. Catenaro, D. M. Rizzo and S. Onori, *Appl. Energy*, 2021, **291**, 116473.
37 Y. Liu, D. Zhang, Y. Shang, Y. Liu and J. Zhang, *J. Electrochem. Soc.*, 2015, **162**, A2123–A2130.
38 J. Li, J. Guo, P. Li, L. Wang and Y. Huang, *Int. J. Electrochem. Sci.*, 2017, **12**, 3212–3220.
39 H. Xiao, Y. Wang, K. Xie, S. Cheng and X. Cheng, *J. Alloys Compd.*, 2018, **738**, 25–31.
40 J. Xiang, P. Zhang, S. Lv, Y. Ma, Q. Zhao, Y. Sui, Y. Ye and C. Qin, *RSC Adv.*, 2021, **11**, 14891–14898.
41 S. Jha, Y. Qin, Y. Chen, Z. Song, L. Miao, Y. Lv, L. Gan and M. Liu, *J. Mater. Chem. A*, 2025, **13**, 15101–15110.
42 Y. Qin, C. Hu, Q. Huang, Y. Lv, Z. Song, L. Gan and M. Liu, *Nano-Micro Lett.*, 2026, **18**, 38.